International Journal of Modern Manufacturing Technologies
ISSN 2067–3604, Vol. XIII, No. 1 / 2021

PROCESS AND REVIEW OF ADDITIVE MANUFACTURED CARGO CARRIERS FOR LOGISTICS APPLICATIONS

Jan Knipschild, Jens Bucher, Dennis Stracke, Bernd Künne

TU Dortmund University, Department of Machine Elements
Leonhard-Euler-Str. 5, 44227 Dortmund, Germany

Corresponding author: Jan Knipschild, jan.knipschild@tu-dortmund.de

Abstract: The trend towards increasing customisation of products requires individual cargo carriers for logistics. Due to the few manufacturing constrains, Additive Manufacturing (AM) is suitable for automated load carrier production. An automated process call for an automated carrier shape generation taking into account application and manufacturing restrictions. The presented algorithm is based on a dexel structure, whereby undercuts are excluded from the beginning. Large product sizes involve big area additive manufacturing (BAAM), including high machine costs and material dosing problems. To reduce costs, a novel BAAM design with a heated hose is proposed and a prototype is generated and manufactured. An accuracy evaluation shows the BAMM system's suitability for the production of cargo carriers.

Key words: additive manufacturing, BAAM, pellet extrusion, cargo carrier, logistics, computational geometry

1. INTRODUCTION

The ongoing trend of product individualisation produces the demand for flexible packaging solutions. Up to now logistics cargo carriers for high quality cargoes are manually designed and built mainly out of wood. To save both time and costs a cargo carrier can be generated and built automatically with Additive Manufacturing (AM). For this AM process a large scale machine is required, which is able to produce a carrier fast and sufficient in terms of resolution.
The advantage of fabrication using AM over milling and turning is that almost any shape can be produced. When milling, the tool may have accessibility restrictions that the AM does not have because the material causing collisions has not yet been placed [9].
Advances in the field of AM have led to reduced production times and increased machine working space. In Fused Deposition Modelling (FDM), pellet extrusion enables higher material throughput than conventional filament extrusion [14]. This leads to shorter production times and comparatively lower material costs for polymer pellets. In addition, pellet-fed AM has a larger range of possible materials [3] including composites and highly flexible polymers [16, 26]. Aside from solid polymers other materials such as polyurethane foams [2] are adapted for the FDM process. These advancements open up new possibilities in logistics to produce custom-made cargo carriers.
Polylactide (PLA), a non-petrochemical polymer which is biodegradable [12], is a suitable AM production material. PLA can also be recycled, whereby after one cycle the mechanical strength is slightly reduced compared to non-recycled material [6, 36]. However, if more than one cycle is performed, the strength decreases continuously with each additional cycle [6].
This paper deals with the automatic shape generation for additive manufactured cargo carriers which is required for an economical process. Initially, cargo geometry data is needed to work with. In AM the STL file format [19] is industry standard, in which geometries are represented by triangulated surfaces, with the triangular facets stored in the form of their three vertices and their normal vectors.
One approach to generate a carrier is the use of Boolean operations by building a rectangular block and subtract the cargo geometry. For this, various algorithms have been published. The general procedure starts with the cut calculation between the body surfaces, which are then divided along the cut's course. The cut surfaces are subsequently combined to a new body according to the chosen Boolean operator. [1]
However, this leads to several problems. Several conditions for the boundary-meshes have to be met when using Boolean operations on boundary-represented geometries, which is why these geometries often need to be pre-processed. Their boundaries has to be closed, hold a volume greater than zero and must not self-intersect [27]. Furthermore, subtraction can lead to a cargo carrier with undercuts.
Using the unmodified cargo geometry will not result in a fitting carrier if the manufacturing deviations are positive. In AM the realizable dimensional accuracy depends on various factors with different impacts. The geometry representation within a STL file is based on

flat triangles, so that curves are approximated by a series of linear segments. The geometric deviation depends on the triangulation's resolution. In addition, in the three-dimensional standard case of AM, the part consists of planar layers of constant thickness, with the production direction orthogonal to the base plane. Consequently, the formation of slopes by stacking layers leads to a staircase effect, which is getting smaller with thinner layers. Moreover, additional geometrical errors are caused by the AM hardware, in particular by the electrical drive resolution and the gear backlash [9]. Furthermore, the manufacturing material behaviour can lead to defects in the finished part. Possible material properties with an impact on the process include viscosity, stickiness and density-temperature behaviour. [31, 32]

To solve the described problems this article proposes an algorithm to generate an undercut free cargo carrier shape taking into account manufacturing tolerances. An example implementation [18] in MATLAB is presented in chapter 3. To evaluate the process, a prototype is produced using a Big Area Additive Manufacturing (BAAM) machine with a novel design that processes polymer granules.

2. STATE OF THE ART

In the following chapter, the state of the art for generating an offset of surface represented geometries is summarised. In addition, BAAM machines and encountered problems are shown.

2.1.Offset geometry surface

Various offset algorithms for triangulated surfaces have been described which can be divided into two subgroups. The first type of algorithm moves the surfaces along their corresponding normal vectors and adjusts the nodes to ensure a closed surface. Each vertex $\boldsymbol{v} \in \mathcal{V}$ has several offset vectors resulting from the individual adjacent facets. The vertex is divided into several new vertices in order to realize all necessary displacements. [17, 21, 25]

The second type considers vertices individually and calculates direction vectors based on the adjacent facets. The offset direction $\boldsymbol{N}^v$ of a vertex $\boldsymbol{v}$ can be calculated as the mean average of the facet's normal vectors $\boldsymbol{N}_i^v$ containing the considered vertex [11].

$$\boldsymbol{N}^v = \frac{\sum_{i=1}^{n} \boldsymbol{N}_i^v}{\left\| \sum_{i=1}^{n} \boldsymbol{N}_i^v \right\|} \tag{1}$$

This approach is mesh dependent, because each facet contributes equally to the resulting offset vector. In order to counteract this mesh dependency, equation (1) can be modified in a way that the facets are weighted by the angles α_i^v between each two edges incident in the considered vertex $\boldsymbol{v}$ [30].

$$\boldsymbol{N}^v = \frac{\sum_{i=1}^{n} \alpha_i^v \boldsymbol{N}_i^v}{\left\| \sum_{i=1}^{n} \alpha_i^v \boldsymbol{N}_i^v \right\|} \tag{2}$$

There are other algorithmic extensions [21] raising the quality of offset surfaces, but also increase the computing time. A desired quality aspect is the avoidance of self-intersections of the computed offset surfaces.

2.2. Big Area Additive Manufacturing (BAAM)

In AM, the polymer is usually fed into the process in form of a pre-processed filament, which is melted in a heating zone and forced through a nozzle by the filament's not yet melted part driven by an drive wheel extruder [23]. The nozzle is moved by a positioning system in the xy-plane horizontally and thus produces the part contours layer by layer. Usually a combination of three linear axes is used, which are driven by stepper motors via belts or lead screws [10].

For various reasons, AM production systems are being developed that use plastic granules instead of a filament, as is the case with other plastic processing methods [34]. Since the intermediate process step is omitted, granulate is a more cost-effective material than filament [20, 21, 34], and the material is exposed to one thermal cycle less, saving energy and reducing stress on the polymer [35]. Furthermore, the use of granules allows a larger variety of materials [3]. This makes it possible to process composite materials with a high proportion of additional components, e.g. carbon fibres, in an AM process, because filaments with a high proportion of fibers cannot be spooled [14]. The conventional AM process has problems with filament buckling between the feed drive and the stem [10, 23, 33]. This limits the processing of filamentary elastomers to hardnesses beyond 70 Shore A [7]. Softer elastomers with hardnesses up to 5 Shore A can be processed in the granular AM process [16, 26].

The processing of granules also has disadvantages. Two types of pellet extruders are used in AM: piston and screw extruders. In a piston extruder, pellets are filled into a cylinder which is heated at its end and tapers to a nozzle. The piston's feed causes the material extrusion. The problem with this design is that there are cavities between the non-melted granules, so that the extruded volume does not correspond to the volume displaced by the piston [34]. Due to the plastic's long residence time in the extruder at high temperature, there is a risk of material damage. In case of polypropylene (PP), which is extruded after a residence time of more than 30 min at 180 °C or more than 10 min at 200 °C and is examined with a Fourier-transform infrared spectrometer, decomposition products can be

detected. However, these do not have a significant influence on the mechanical properties [34].

The more common extruder design is the screw extruder, which is also used in various other manufacturing processes, such as injection moulding, wire coating, tubular film blowing, and blow moulding [28]. A screw extruder consists of a heated barrel with a screw comprising different zones. The still solid pellets are transported through the screw's front part into the melting zone where the material is compressed and melted. In the screw's rear part, the metering section, the liquid plastic is pumped out of the extruder. [4]

The AM uses single-screw extruders in various sizes. Extruders for desktop-sized machines have screw dimensions of approx. 18×125 mm [3] and 15.5×180 mm [16]. The largest screw extruders are used in Big Area Additive Manufacturing (BAAM), where one screw is approximately 610 mm long [29].

Screw extruders also have the problem that, as the material's residence time in the extruder increases, it decomposes [20]. In contrast to the screw extruder's usual field of application, the AM screw extruder is not operated in a stationary state, but has to start and stop frequently and, for example, reduce the material's volume flow when cornering [5]. In a screw extruder the material feed is not determined by the displacement of a volume, so the volume flow is caused by an interaction between the polymer and the screw [5]. The screw is surrounded by the polymer and supported by it, which, driven by the pressure gradient, creates a backflow [28].

The advantages of granulate extruders are particularly evident if BAAM is used. On the one hand, the lower material costs are more significant manufacturing larger parts and on the other hand, higher construction rates are possible. The limiting factor with filament machines is the heating of the material to a temperature above the glass transition temperature near the melting temperature. If the temperature is not reached over the entire radius, the extrusion force increases and can lead to failure of the filament feed in severe cases. With a filament extruder, melting has to take place in a small zone, as the still solid filament is required as a piston for extrusion. Heat is transferred by heat conduction through the shaft's wall. Polymers are generally poor heat conductors, so that the time required for heating through limits the extrusion speed [10].

An approach to accelerate filament extrusion was developed by *Go and Hart* [10]. They use a laser to heat the filament in a shorter time. When using pellets, other extruders are used which do not depend on solid material, so that more time is available for melting.

A special case of AM is BAAM, as the defects are more evident there [5], as the material flow cannot be stopped abruptly, surplus material is extruded and defects can occur. Therefore, *Love et. al.* [20] carry out a spiral movement with the print head before jumps without material flow in order to level excess material. The problem in this case is not only the complete standstill, but also the dynamic adjustment while depositing a bead. The mass flow has to be reduced before driving a curve and increased again afterwards. If a large screw extruder is controlled in the same way as a conventional filament feeder, incorrect metering will occur. *Chesser et. al*. [5] created an empirical extruder model to describe the relationship between the changes in speed and volume flow and installed a bypass valve that drains excess material before it comes out of the nozzle.

A larger nozzle diameter allows a higher material flow, but increases the inherent deviations of AM [5, 9]. It is therefore advisable to use large nozzle diameters only where low geometrical accuracy is acceptable. One way to increase the application of large nozzle diameters is to use different nozzle diameters during the production of a single component. This makes it necessary to change nozzles quickly. *Chesser et. al.* [5] developed a nozzle for this purpose which can adjust two different effective diameters by moving a cone inside the nozzle. In their specific application, it is possible to produce moulds for the manufacturing of car body parts, whereby the actual mould, because of its higher precision requirements, is produced with a smaller nozzle than the other outer contours.

3. GEOMETRY GENERATION

The carrier's shape has to be designed in a way that the cargo can be inserted from above, so undercuts must be avoided. To discretise the cargo carrier a dexel structure is chosen, where a set of parallel dexel emerge from a discretised plane and approach the cargo from one direction. Each dexel either hits the cargo's surface, in which its first spatial coordinate of collision is recorded, or misses. In theory, an algorithmic implementation of this model meets all the requirements imposed on a cargo carrier. However, because of the aforementioned process' intrinsic tolerances, a surface offset is added to the cargo geometry. This positive offset ensures that the cargo fits into the cargo carrier after the manufacturing process. The resulting workflow is shown in Figure 1. Initially, a surface representation of the cargo must be created. If CAD data is not available, reverse engineering strategies are required, e.g. using a 3D scanner. At the algorithm's beginning the cargo geometry is loaded and transformed into an index referencing structure for easier use. Afterwards the offset is applied and intersections between a dexel structure and the cargo surface are calculated. From the obtained intersection points a clean triangulation is created. In three dimensions, therefore not shown in the figure, the last step is the marginal surface generation, so that a rectangular cargo carrier is created.

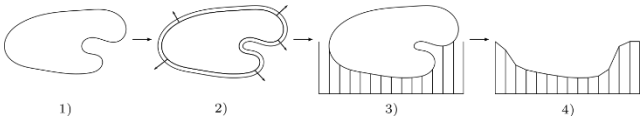

Fig. 1. Algorithm concept: 1) Obtaining and loading the cargo geometry, 2) Applying the offset, 3) Determining the intersection points, 4) Triangulation of the contact surface

The STL geometry file is loaded using an algorithm by *Johnson* [15], which returns the sets of facets $\mathcal{F}$, vertices $\mathcal{V}$ and normal vectors $\mathcal{N}$. The geometry's surface is represented by k facets containing l vertices. The facets are stored in a $k \times 3$ matrix, where each row contains the facet's three defining vertices. The matrix with the vertex information has the dimensions $l \times 3$, where the columns correspond to the coordinate axes x, y and z.

Consequently, the vertices are moved in the vector's direction calculated with equation (2). There are other algorithmic extensions [21] that increase the quality of offset surfaces, however, this is not necessary for this particular application. Self-intersections caused by the offset have no influence on the further generation, so that simplicity and less computing time are preferred here.

Then the contact surface between the cargo carrier and the cargo is approximated with the dexel structure. The origin points $\mathcal{P} \subseteq \mathbb{R}^3$ are arranged in a plane grid parallel to the xy-plane, whose constant z-coordinate z_0 is chosen accordingly to the resulting cargo carrier's desired bottom thickness t_b. The relationship between t_b and z_0 is given by

$$z_0 = min\{v_z : \forall \boldsymbol{v} = (v_x, v_y, v_z) \in \mathcal{V}\} - t_b, \quad (3)$$

where v_i is the i-th component of a vertex $\boldsymbol{v}$ in the set of vertices $\mathcal{V}$. Except for memory and performance considerations, the grid points can be defined using arbitrary resolutions in the coordinate directions.

Without loss of generality, the positive dexel depth direction is the z-axis, such that for each $\boldsymbol{p} \in \mathcal{P}$ a ray is defined by

$$g^p(t) = \boldsymbol{p} + t \cdot \begin{pmatrix} 0 \\ 0 \\ 1 \end{pmatrix}, t > 0, \quad (4)$$

Furthermore, g_z^p denotes the ray's z component of g^p and let

$$\mathcal{I}_z^p = \{g_z^p(t_i) : t_i \text{ such that } g^p(t_i) \text{ intersects } f \in \mathcal{F}\} \quad (5)$$

define the set of all z-values per origin point $\boldsymbol{p} \in \mathcal{P}$ of intersection points of $g^p(t)$ with cargo model facets. The dexel depth d_p for each origin point $\boldsymbol{p} \in \mathcal{P}$ is then computed with

$$d_p = \begin{cases} \left\lfloor \frac{min\{\mathcal{I}_z^p\}}{r_z} \right\rfloor r_z & \text{, if } \mathcal{I}_z^p \neq \emptyset \\ max(d_p) & \text{, if } \mathcal{I}_z^p = \emptyset \end{cases} \quad (6)$$

where r_z is the AM layer height. This definition ensures that no carrier structures are created that extend into the component and takes the AM process' intrinsic layer discretisation into account. The presented geometric measures are visualized in Figure 2.

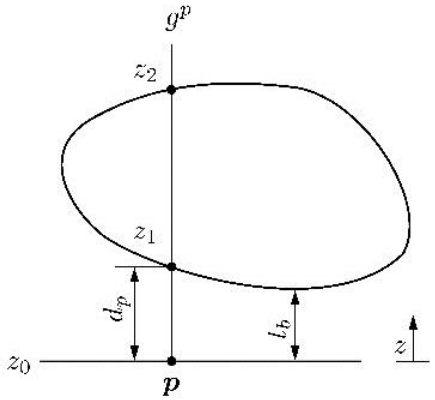

Fig. 2. Geometric measures in the dexel structure, where $z_1, z_2 \in \mathcal{I}_z^p$

If a dexel has no intersection with a surface, the dexel depth is set to the maximum depth of all cut dexels.

Calculating the intersection points is a time-consuming operation and should therefore be carried out efficiently. Thus, the proposed algorithm uses a form of pull-back to transform these time-intensive operations into a two dimensional problem. After these calculations have been finished, the results are transformed back into three dimensions.

Initially, all input geometry facets $f \in \mathcal{F}$ and all points $\boldsymbol{p} \in \mathcal{P}$ are projected onto the xy-plane by setting the z-component of each corresponding vertex to zero, and let $\alpha: \mathcal{F} \to \mathcal{F}_{xy}$ be this projection map onto the set of plane triangles $\mathcal{F}_{xy}$. Although α is not an one-to-one mapping in a strict mathematical sense, its inverse α^{-1} can be built by storing the eliminated z-component before projection.

Using an AABB-tree [8], for each $\boldsymbol{p} \in \mathcal{P}$ the subset $\mathcal{F}_p \subseteq \mathcal{F}_{xy}$ that contains all projected facets, which contain $\boldsymbol{p}$, and the individual barycentric coordinates are calculated.

The z-coordinates g_z^p are then determined by barycentric interpolation. Considering a dexel g^p and an arbitrary facet $f \in \mathcal{F}_p$, in a first step the corresponding vertices $\boldsymbol{v}_1, \boldsymbol{v}_2, \boldsymbol{v}_3 \in \mathcal{V}$ of the facet $\alpha^{-1}(f) \in \mathcal{F}$ are calculated. The intersection point's z-coordinate is then determined by evaluating the formula

$$g_z^p(f) = \sum_{j=1}^{3} v_{j,z} a_j, \quad (7)$$

where a_j is the barycentric coordinate describing the intersection position in the xy-plane. Finally, let $\beta: \mathcal{P} \to \mathcal{F}$ be a map such that

$$\beta(\boldsymbol{p}) = \begin{cases} a^{-1}(f), g_z^p(f) \text{ minimal for all } f \in \mathcal{F}_p \\ \emptyset, \ \mathcal{F}_p = \emptyset \end{cases} \quad (8)$$

and

$$I = \bigcup_{\boldsymbol{p} \in \mathcal{P}} \beta(\boldsymbol{p}) \,. \quad (9)$$

Because there are no requirements defined with respect to the input STL file, it is possible that β could be not well-defined. Thus, in the case where there exist multiple facets $\boldsymbol{f}$ with g_z^p minimal, the first facet found is chosen as the map's image.

In view of parts with small overhangs at the upper end, it is reasonable not to support such structures, because this results in unnecessarily large cargo carriers. Therefore, a support ratio s is defined and the maximum height is then calculated as

$$h_{\max} = g_z^p(\tilde{I})_{[s \cdot \#\tilde{I}]}, \quad (10)$$

where $\tilde{I}$ is a permutation of I, such that all elements $g_z^p(\tilde{I})$ are ordered in an ascending fashion.

In the last step, a modified z-value (i.e. the final dexel depth) for each $\boldsymbol{p} \in \mathcal{P}$ is calculated by a modified form of equation (6):

$$d_p = \begin{cases} \left\lfloor \frac{min\{\mathcal{I}_z^p \cup \{h_{\max}\}\}}{r_z} \right\rfloor r_z & , \text{if } \mathcal{I}_z^p \neq \emptyset \\ h_{\max} & , \text{if } \mathcal{I}_z^p = \emptyset. \end{cases} \quad (11)$$

Grid points $\boldsymbol{p} \in \mathcal{P}$ are arranged in a mesh grid data structure, i.e. two matrices $\mathbf{P}_\mathrm{x}$ and $\mathbf{P}_y$ of dimension $m \times n$ with m and n being the required amounts of grid points with respect to the chosen discretisation resolutions r_x and r_y. Accordingly, the matrix $\mathbf{P}_z$ holds the calculated dexel depths d_p, such that for an arbitrary $\boldsymbol{p} \in \mathcal{P}$ with x-coordinate $p_x = \mathbf{P}_\mathrm{x}(i_0, j_0)$ and y-coordinate $p_y = \mathbf{P}_\mathrm{y}(i_0, j_0)$ the equation $z_p^{\min} = \mathbf{P}_\mathrm{z}(i_0, j_0)$ is fulfilled.

The matrix $\mathbf{P}_z$ forms a quadrilateral surface mesh with the xy-coordinates of the origin points $\mathcal{P}$, which has to be triangulated. A quadrilateral surface mesh can be converted to a triangulation mesh by dividing the quads into two triangles each by either forward slash or back slash. An algorithmic implementation by *Moerman* [22] is used.

An arbitrary quad in the grid located between the points (m, n) and $(m+1, n+1)$ is split into two triangles with the resulting new connectivity matrix $\mathbf{f}_n$.

$$\mathbf{f}_n = \begin{pmatrix} (m, n+1) & (m+1, n) & (m, n) \\ (m+1, n+1) & (m+1, n) & (m, n+1) \end{pmatrix}. \quad (12)$$

In order to obtain an easy-to-use data structure, the two-dimensional indices are converted into one-dimensional indices. Besides, a list of vertices is built from the matrices $\mathbf{P}_\mathrm{x}$, $\mathbf{P}_\mathrm{y}$ and $\mathbf{P}_\mathrm{z}$. Thus, the structure with facets referencing vertices is achieved.

A closed volume is formed from the contact surface with an algorithm by *Holcombe* [13]. At first, the surface's boundary edge is extracted. The carrier base layer is constructed by duplicating the vertices and setting the z-coordinates to the bottom height z_0. The outer walls are defined by the base layer's boundary and the contact surface's edge. After that, the wall facets are connected to obtain triangles. Finally, the individual surfaces are combined to form the finished model.

To strap down the cargo with the carrier to a pallet, tension belts can be used. If additional protection against slippage on the pallet is needed two tunnels for fixation belts can be added. For an AM-compliant model, the tunnels are triangular with a 45° angle at the tip, thus meeting the overhang constraint.

The algorithm's MATLAB implementation is distributed under the GNU GPL license [18]. The source code is optimised in terms of runtimes. To keep computing times low, most operations are applied directly to all vertices or facets, avoiding loops.

4. BAAM SYSTEM

In order to continue the developments by *Khondoker et. al.* [16] and *Chesser et. al.* [5], a novel AM system is built and tested. The system combines a flexible hose with BAAM and uses a gear pump located upstream the nozzle for precise dosing. The material, deposited by the AM system, enters the process in the form of pellets. To minimize denaturation during the melt preparation process, the material must be dried first. From the dryer, the pellets are fed into the screw extruder by means of a vacuum conveyor. The melt leaves the screw extruder and is conveyed via a heated flexible tube with a length of 3 m to the gear pump. The pump outlet narrows continuously without diameter jumps to a nozzle with a diameter of 3 mm.

From the point at which the pellets are melted, all process components are heated to ensure the melt transport. The temperature of the flexible tubing, the pump flanges, and the pump itself can be controlled individually. The flange at the pump outlet holds the nozzle, so that the nozzle temperature is controlled together with the flange temperature. For control and monitoring purposes, the melt pressure is measured downstream of the screw extruder and upstream and downstream of the gear pump.

In order to ensure that the deposited material retains its desired shape, it must be cooled below the melting temperature as quickly as possible. For this purpose, two controllable axial fans are mounted near the nozzle.

The experimental AM system which is illustrated in Figure 3, consists of three linear axes arranged in a

gantry kinematic system, where the supporting structure is made out of aluminium profiles. The bridge runs on a linear bearing and is driven via a belt by a servo motor with a downstream gearbox. On the bridge, a gear pump is mounted, which can be moved via a drive train consisting of a servo motor, a gearbox and a belt drive. The pump itself is driven by another servo motor with a downstream angular gear. The gear pump is heated and, as shown in Figure 4, thermally separated from the bridge by insulation. The heated bed can be adjusted in height by a spindle and is supported by three cylindrical guides. The AM system has a workspace of $935 \times 635 \times 450$ mm.

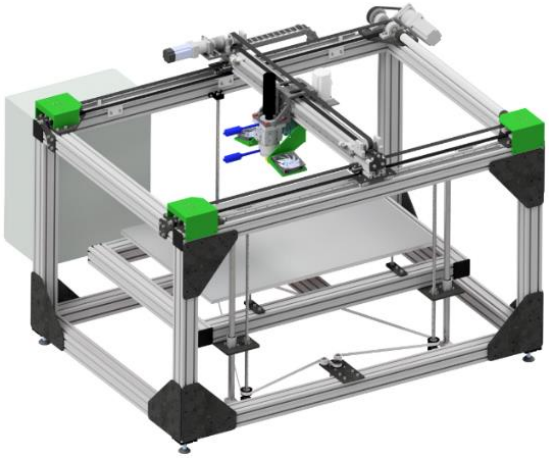

Fig. 3. Overall construction

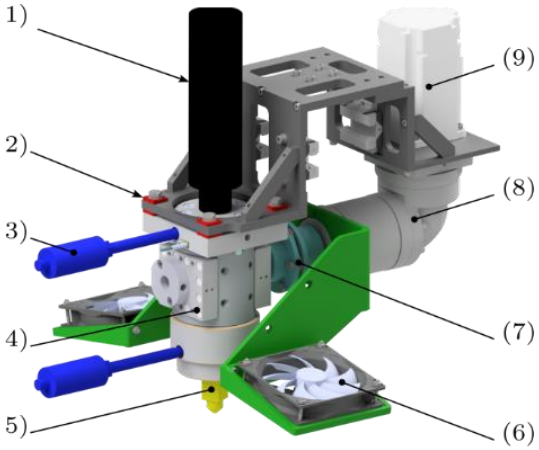

Fig. 4. Print head: (1) Heated flexible tube, (2) Thermal insulation, (3) Pressure sensor, (4) Gear pump, (5) Nozzle, (6) Fans, (7) Clutch, (8) Gearbox (9) Servo motor

If no gear pump is used and the mass flow is stopped, the flexible hose acts as a melt buffer due to its elastic compliance. To reduce the pressure at the nozzle, the inert screw extruder's direction of rotation must be reversed. During this time, the print head stands still and the melt continues to flow. In addition, the pressure in the hose has to be built up first during start up, in order to achieve the desired mass flow. A gear pump in the direct proximity of the nozzle eliminates the flexible tube's transient mass flow effects from the controlled system, so that the mass flow can be adjusted or stopped within a short time.

During AM, no stationary state is achieved at the nozzle, as mass flow adjustments are constantly required and the nozzle back pressure changes depending on whether the print head is moved over solidified material or in free space. Therefore, the mass flow cannot be controlled by a pressure regulation at the nozzle. With constant inlet pressure the mass flow depends mainly on the pump speed, while the nozzle back pressure has only a small influence. Hence the pump's speed is controlled in the process. The relationship between pump speed and mass flow for the material used is determined by placing a continuous logging scale under the print head, as different speeds in the range of 0 to 15 rpm are set with a regulated pump inlet pressure of 20 bar. A linear regression model determines the relationship between the mass flow $\dot{m}$ in g/s and the pump speed n in rpm to

$$\dot{m} = 0.0884 \cdot n + 0.0088 \qquad (13)$$

where a coefficient of determination of $R^2 = 0.9994$ is achieved.

5. PROTOTYPE

For the process evaluation a cargo carrier for an automotive shock absorber is produced. The geometry combines round, angular and flat structures, which would lead to undercuts in a cargo carrier created with Boolean operations.

The surface data is obtained using the Artec Eva 3D-Scanner and the accompanying software Artec Studio 15.

By applying the described algorithm with an offset of 8 mm, a wall thickness of 10 mm, a floor thicknesses of 5 mm and a dexel structure resolution of 1 mm in all spatial directions, the cargo carrier geometry is generated. From the chosen resolution and the cargo's bounding box results a 611×222 grid with a total of 135,642 dexels. The support ratio is set to $s = 0.97$, so that the flange's upper edge is not supported. Through the algorithm a carrier with a height of 115 mm is generated. The surface consists of 272,952 vertices connected to form 545,900 facets. The mean runtimes for each individual algorithm step, obtained from three consecutive code executions, are shown in Table 1. The reference system is equipped with MATLAB version 2020b, an Intel Core i9-10900 CPU and 32 GB of RAM. In Figure 5 the shock absorber is shown in red, which is encapsulated by the offset surface.

Table 1. Algorithm execution times

Step	Mean duration [s]
Load STL	1.90
Apply offset	1.12
Determine intersection points	1.98
Triangulate surface	0.01
Generate marginal surface	0.07

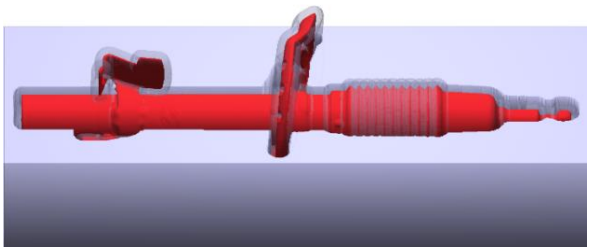

Fig. 5. Shock absorber with transparent offset surface and the resulting cargo carrier

As the manufacturing material PLA 4043D [24] granulate from NatureWorks LLC is used, which has a melt flow rate (MFR) of 6 g/10 min at 210 °C with a load of 2.16 kg (ASTM D1238). The melting temperature is indicated as the range of 145-160 °C.
In the manufacturing process, quality settings with a layer height of 1 mm and a line width of 3 mm are used. Hence, the ratio of nozzle diameter to layer width is 1. Each layer is surrounded by two perimeters. Inside, infill is used with a gyroid pattern and a density of 15 %. Furthermore, a bottom layer and five top layers are used. To suppress a seam, the starting point of each layer is randomly chosen between the outer corners. A speed of 180 mm/s is selected. The retraction distance is 40 mm with a related speed of 4000 mm/s and is required for travel distances of more than 25 mm. The screw extruder controls to a pump inlet pressure of 20 bar, the same as used for determining the characteristic curve.
The cargo carrier's manufacturing takes three hours of time, in which 5.7 kg of material is deposited in 115 layers. The produced part is shown in Figure 6.
It is possible to put the shock absorber in the carrier, even if some defects are visible.

Fig. 6. Cargo carrier fabricated with AM

To analyse the deviations, the prototype is 3D scanned and compared to the source model using the software Cloudcompare V2.11.3. The colour coded deviations and the deviation distribution are shown in Fig. *7*. From the analysis a mean deviation of 0.47 mm is obtained, with 90 % of deviations observed within the interval ± 1.500 mm.

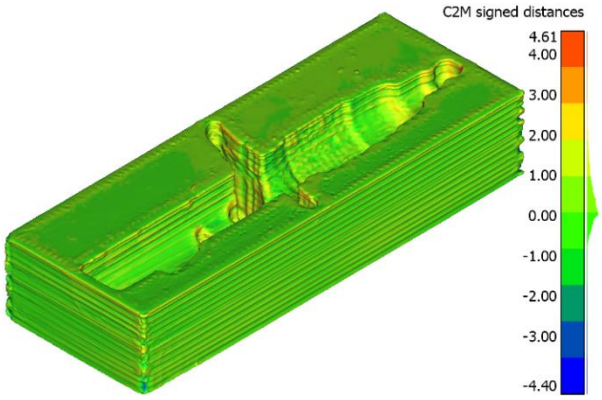

Fig. 7. Cargo carrier shape deviation

The larger defects are mainly concentrated in the outer corners and differ in intensity in the different layers. The corners are recessed, if they are the starting point of a new layer caused by the time delay before material extrusion begins. Due to the random start point localization in the outer corners, irregular edges are formed. Smaller material accumulations are visible in sharp corners, e.g. on the top layer at the perimeters, caused by the zig-zag skin pattern.

6. DISCUSSION

The proposed algorithm does not depend on a watertight model and can therefore take any surfaces positioned in space as input, as long as the normal vectors are oriented properly. By design, it is impossible that the generated output triangulation contains degenerated or overlapping facets or non-manifold topology conditions. This is achieved, because of the equal intersection points' grid arrangement in the xy-plane, which forms the cargo carrier contact surface. After triangulating the intersections to form the carrier, the connectivity list of the facets is independent of the input geometry and well defined. Since the surface is newly triangulated by the intersection points, it is only a contour approximation that depends on the grid resolution. However, this is compensated through the achieved clean triangulation.
Problems arise with cargo geometries that have no overhang, e.g. with geometric bodies such as cubes, vertical cylinders, cones or pyramids. In such a case the algorithm produces a single rectangular block, so there is no lateral support. Sufficient lateral support can be achieved by defining a required minimum depth for uncut dexels.
The cargo geometry's surface offset creates self-intersections, but this has no influence on the further cargo carrier generation. For the practical application, the possibility, to work with incomplete cargo representations, is a huge advantage. A great amount of time can be saved by the possibility to 3D-scan the desired contact surface, without the need of further

work like scanning the whole cargo or repairing the produced scan data to make the model watertight.
The printed prototype shows two things. First the generated cargo carrier can be fed into the classical AM workflow by slicing the geometry and generating a GCODE used to control the AM system. The generation workflow's errors are smaller than 8 mm so the cargo can be placed inside. The
AM system design is capable of performing sufficiently in terms of accuracy for a low cost system in logistics. Furthermore, material costs were reduced by a factor of 2.5 by using polymer granulate instead of filament. To reduce the manufacturing errors further, the pump has to extrude additional material after travel moves. To be able to produce more complicated and more detailed geometries, a smaller nozzle diameter has to be used and the AM system has to be further enhanced, e.g. with a stiffer frame.
The heated flexible tube is a suitable possibility to reduce frame and motor costs. Because of the large heated distance, a minimum print speed is necessary to reduce the residence time and therefore material decomposes.
The cargo carrier is stable, but heavy. The resistance of the carrier comes from the broad deposited beads, due to the selected nozzle diameter. Furthermore, because of the large bead cross section, a lot of heat energy is stored, so that layer bonding is improved. Therefore, no carrier damage is expected from holding the cargo.
In comparison to the shock absorber's mass of 4.2 kg the carrier is too heavy with the accompanying disadvantages of high material usage and a long built time. In order to reduce the mass, a nozzle with a smaller diameter in combination with thinner walls could be used in the production of the carrier. In addition, the shape of the carrier could be adapted to cut out superfluous geometric parts, e.g. by topology optimisation. These adjustments make it necessary to verify whether the carrier can still withstand the transport stresses.

7. CONCLUSIONS

In this report, AM was proposed for logistics carrier production and an algorithm for automatic carrier shape generation was presented and tested. The dexel structure based algorithm is able to work with non-waterproof and self-intersecting geometry surfaces and outputs a clean triangulated carrier geometry without undercuts. In addition, manufacturing tolerances are compensated within the shape generating process. A BAAM system was presented, while the costs for the drives and the frame could be kept at a low level as the moving mass was reduced by using a heated flexible tube. With the developed system a cargo carrier prototype, derived from the 3D scan of an automotive shock absorber, was manufactured successfully. For evaluation a 3D scan of the carrier was performed and the surface distances to the source model were calculated. 90% of the deviations were in a symmetrical interval with a spacing of half the nozzle diameter in each direction. Larger defects could be explained by under-extrusion after traveling. Due to these facts, it is possible to draw the conclusion that the BAAM system, in combination with the algorithm, is capable of generating logistics cargo carriers.

8. ACKNOWLEDGEMENTS

This research was funded by the federal state of North Rhine-Westphalia and the "European Regional Development Fund" (ERDF 2014-2020) under Grant No. EFRE-0800854.
The authors thankfully acknowledge the Kremer Machine Systems GmbH for the screw extruder's loan.

9. REFERENCES

1. Barki, H., Guennebaud, G., Foufou, S. (2015). *Exact, robust, and efficient regularized Booleans on general 3D meshes*, Computers & Mathematics with Applications, **70**(6), 1235-1254.
2. Barnett, E., Gosselin, C. (2015). *Large-scale 3D printing with a cable-suspended robot*, Additive Manufacturing, **7**, 27-44.
3. Bellini, A., Shor, L., Guceri, S. I. (2005). *New developments in fused deposition modeling of ceramics*, Rapid Prototyping Journal, **11**(4), 214-220.
4. Campbell, G. A., Spalding, M. A. (Eds.) (2013). *Analyzing and Troubleshooting Single-Screw Extruders*, Carl Hanser Verlag GmbH & Co. KG, München.
5. Chesser, P., Post, B., Roschli, A., Carnal, C., Lind, R., Borish, M., Love, L. (2019). *Extrusion control for high quality printing on Big Area Additive Manufacturing (BAAM) systems*, Additive Manufacturing, **28**, 445-455.
6. Cruz Sanchez, F. A., Boudaoud, H., Hoppe, S., Camargo, M. (2017). *Polymer recycling in an open-source additive manufacturing context: Mechanical issues*, Additive Manufacturing, **17**, 87-105.
7. Elkins, K., Nordby, H., Janak, C., Gray IV, R. W., Helge Bohn, J., Baird, D. G. (1997). *Soft elastomers for fused deposition modeling*, 1997 International Solid Freeform Fabrication Symposium.
8. Engwirda, D. *FINDTRIA: Point-In-Simplex Queries in R^d: GitHub repository*. Available from *https://github.com/dengwirda/find-tria*, Accessed: 28/10/2020.
9. Gibson, I., Rosen, D., Stucker, B. (2015). *Additive Manufacturing Technologies*, Springer New York, New York, NY.
10. Go, J., Schiffres, S. N., Stevens, A. G., Hart, A. J. (2017). *Rate limits of additive manufacturing by fused filament fabrication and guidelines for high-*

throughput system design, Additive Manufacturing, **16**, 1-11.
11. Gouraud, H. (1971). *Continuous Shading of Curved Surfaces*, IEEE Trans. Comput., **C-20**(6), 623-629.
12. Gupta, B., Revagade, N., Hilborn, J. (2007). *Poly(lactic acid) fiber: An overview*, Progress in Polymer Science, **32**(4), 455-482.
13. Holcombe, S. *surf2solid - make a solid volume from a surface for 3D printing: MATLAB Central File Exchange*. Available from *https://de.mathworks.com/matlabcentral/fileexchange/42876-surf2solid-make-a-solid-volume-from-a-surface-for-3d-printing*, Accessed: 28/10/2020.
14. Holshouser, C., Newell, C., Palas, S., Love, L. J., Kunc, V., Lind, R. F., Lloyd, P. D., Rowe, J. C., Blue, C. A., Duty, C. E., Peter, W. H., Dehoff, R. R. (2013). *Out of bounds additive manufacturing*, Advanced Materials and Processes, **171**(3).
15. Johnson, E. *STL File Reader: MATLAB Central File Exchange*. Available from *https://de.mathworks.com/matlabcentral/fileexchange/22409-stl-file-reader*, Accessed: 28/10/2020.
16. Khondoker, M. A. H., Sameoto, D. (2019). *Direct coupling of fixed screw extruders using flexible heated hoses for FDM printing of extremely soft thermoplastic elastomers*, Prog Addit Manuf, **4**(3), 197-209.
17. Kim, S.-J., Lee, D.-Y., Yang, M.-Y. (2004). *Offset Triangular Mesh Using the Multiple Normal Vectors of a Vertex*, Computer-Aided Design and Applications, **1**(1-4), 285-291.
18. Knipschild, J., Stracke, D. *loadcarrier: GitHub repository*. Available from *https://github.com/janknipschild/loadcarrier*, Accessed: 28/10/2020.
19. Le Roscoe, others (1988). *Stereolithography interface specification*, 3D Systems Inc.
20. Love, L. J., Duty, C. (2015). *Cincinnati big area additive manufacturing (BAAM)*, Oak Ridge.
21. Malosio, M., Pedrocchi, N., Tosatti, L. M. (2009). *Algorithm to Offset and Smooth Tessellated Surfaces*, Computer-Aided Design and Applications, **6**(3), 351-363.
22. Moerman, K. *mesh2tri: MATLAB Central File Exchange*. Available from *https://de.mathworks.com/matlabcentral/fileexchange/28327-mesh2tri*, Accessed: 28/10/2020.
23. N. Turner, B., Strong, R., A. Gold, S. (2014). *A review of melt extrusion additive manufacturing processes: I. Process design and modeling*, Rapid Prototyping Journal, **20**(3), 192-204.
24. NatureWorks LLC. *Ingeo™ Biopolymer 4043D Technical Data Sheet*. Available from *https://www.natureworksllc.com/~/media/Files/NatureWorks/Technical-Documents/Technical-Data-Sheets/TechnicalDataSheet_4043D_3D-monofilament_pdf.pdf*, Accessed: 28/10/2020.
25. Qu, X., Stucker, B. (2003). *A 3D surface offset method for STL- format models*, Rapid Prototyping Journal, **9**(3), 133-141.
26. Saari, M., Galla, M., Cox, B., Krueger, P., Cohen, A., Richer, E. (2015). *Additive manufacturing of soft and composite parts from thermoplastic elastomers*, Solid Freeform Fabrication Symposium, pp. 949-958.
27. Sâm Landier (2015). *Boolean Operations on Arbitrary Polyhedral Meshes*, Procedia Engineering, **124**, 200-212.
28. Stevens, M. J., Covas, J. A. (1995). *Extruder Principles and Operation*, Springer Netherlands, Dordrecht.
29. Sudbury, Z., Duty, C., Kunc, V., Kishore, V., Ajinjeru, C., Failla, J., Lindahl, J. (2016). *Characterizing Material Transition for Functionally Graded Material Using Big Area Additive Manufacturing*, 27th Annual International Solid Freeform Fabrication Symposium. Austin, TX.
30. Thürmer, G., Wüthrich, C. A. (1998). *Computing vertex normals from polygonal facets*, Journal of Graphics Tools, **3**(1), 43-46.
31. Turner, B. N., Gold, S. A. (2015). *A review of melt extrusion additive manufacturing processes: II. Materials, dimensional accuracy, and surface roughness*, Rapid Prototyping Journal, **21**(3), 250-261.
32. van Weeren, R., Agarwala, M., Jamalabad, V. R., Bandyopadhyay, A., Vaidyanathan, R., Langrana, N., Safari, A., Whalen, P., Danforth, S. C., Ballard, C. (1995). *Quality of parts processed by fused deposition*, 1995 International Solid Freeform Fabrication Symposium.
33. Venkataraman, N. (2000). *The process-property-performance relationships of feedstock materials used for fused deposition of ceramics (FDC)*, New Brunswick.
34. Volpato, N., Kretschek, D., Foggiatto, J. A., Gomez da Silva Cruz, C. M. (2015). *Experimental analysis of an extrusion system for additive manufacturing based on polymer pellets*, Int J Adv Manuf Technol, **81**(9-12), 1519-1531.
35. Woern, A. L., Byard, D. J., Oakley, R. B., Fiedler, M. J., Snabes, S. L., Pearce, J. M. (2018). *Fused Particle Fabrication 3-D Printing: Recycled Materials' Optimization and Mechanical Properties*, Materials (Basel, Switzerland), **11**(8).
36. Woern, A. L., McCaslin, J. R., Pringle, A. M., Pearce, J. M. (2018). *RepRapable Recyclebot: Open source 3-D printable extruder for converting plastic to 3-D printing filament*, HardwareX, **4**, e00026.

Received: December 11, 2020 / Accepted: June 15, 2021 / Paper available online: June 20, 2021